

We are IntechOpen, the world's leading publisher of Open Access books Built by scientists, for scientists

6,900

Open access books available

186,000

International authors and editors

200M

Downloads

Our authors are among the

154

Countries delivered to

TOP 1%

most cited scientists

12.2%

Contributors from top 500 universities



WEB OF SCIENCE™

Selection of our books indexed in the Book Citation Index
in Web of Science™ Core Collection (BKCI)

Interested in publishing with us?
Contact book.department@intechopen.com

Numbers displayed above are based on latest data collected.
For more information visit www.intechopen.com



Optical Chirality and Single-Photon Isolation

Lei Tang and Keyu Xia

Abstract

Optical isolation is important for protecting a laser from damage due to the detrimental back reflection of light. It typically relies on breaking Lorentz reciprocity and normally is achieved via the Faraday magneto-optical effect, requiring a strong external magnetic field. Single-photon isolation, the quantum counterpart of optical isolation, is the key functional component in quantum information processing, but its realization is challenging. In this chapter, we present all-optical schemes for isolating the backscattering from single photons. In the first scheme, we show the single-photon isolation can be realized by using a chiral quantum optical system, in which a quantum emitter asymmetrically couples to nanowaveguide modes or whispering-gallery modes with high optical chirality. Secondly, we propose a chiral optical Kerr nonlinearity to bypass the so-called dynamical reciprocity in nonlinear optics and then achieve room-temperature photon isolation with low insertion loss. The concepts we present may pave the way for quantum information processing in an unconventional way.

Keywords: single-photon isolation, optical chirality, chiral light-matter interaction, optical isolator, optical circulator, chiral Kerr nonlinearity

1. Introduction

Controlling the flow of light is extremely essential for quantum information processing in integrated optical circuits. Nonreciprocal propagation of light at the single-photon level is in great demand for applications in quantum networks [1, 2], quantum computing [3], quantum entanglement [4], and quantum measurement [5]. For this purpose, nonreciprocal photonic elements, such as optical isolators and circulators, processing and routing of photonic signals at ultralow light level, or single-photon level in integrated optical circuits has been attracting a lot of interest.

The conventional implementations of nonreciprocal optical devices are achieved by using the Faraday magneto-optical effect. However, such Faraday-effect-based devices suffer large optical losses and conflict with miniaturization and integration. To date, integrated nonreciprocal photonic elements have been demonstrated via magneto-optical effect [6, 7], optical nonlinearity [8–10], and opto-mechanical system [11–13]. Very recently, Dong et al. proposed and experimentally realized a scheme to achieve a true single-photon non-reciprocity in a cold atomic ensemble [14]. However, most of these devices cannot achieve high isolations, low losses, and compatibility with single-photon level at the same time.

Nanophotonic devices control and confine the flow of light at a subwavelength scale. The strong confinement in these structures yields optical chirality, which is an inherent link between local polarization and the propagating direction of light [15]. If quantum emitters are embedded in these structures, chiral light-matter interaction is obtained, leading to propagation-direction-dependent emission, absorption, and scattering of photons. As a result, chiral light-matter interaction can be used to break time symmetry and achieve on-chip single-photon isolation. Some feasible schemes based on chiral quantum optics have been proposed to realize non-reciprocity at the single-photon level [16, 17], and optical isolators and circulators have been experimentally demonstrated in full quantum regime [18, 19].

Besides strong confinement of light, atoms can induce optical chirality. Here, optical chirality is chiral cross-Kerr (XKerr) nonlinearity induced in atoms. As a result of the chirality of atomic nonlinearity, the phases and transmission amplitudes of the forward- and backward-moving probe fields are sufficiently different after passing through atoms in two opposite directions. Thus, chiral XKerr nonlinear can achieve chip-compatible optical isolation with high isolation and low insert losses [20]. And very recently, XKerr-based optical isolators and circulators for high isolation, low loss, and an ultralow probe field at room temperature have been experimentally demonstrated [21].

2. Optical chirality and chiral light-matter interaction

The strong light confinement in subwavelength structures, e.g., nanofibers, nanowaveguides, or whispering-gallery mode (WGM) microresonators, can lock the local polarization of the light to its propagation direction. In these structures, the light is strongly confined transversely, leading to a longitudinal component of the electric field (e-field), which is parallel with the propagation direction. The longitudinal and transverse components, denoted as \mathbf{E}_{\parallel} and \mathbf{E}_{\perp} , respectively, are comparable, and the former oscillates $\pm\pi/2$ radians out of phase with respect to the latter, with the \pm sign depending on the propagation direction of the light (forward or backward) [15]:

$$\mathbf{E}_{\text{local}} = \mathbf{E}_{\perp} \pm i\mathbf{E}_{\parallel} . \quad (1)$$

As a consequence, the local polarization of the light is elliptical, yielding a transverse spin angular momentum component, whose e-field rotates around an axis perpendicular to the propagation direction. The transverse spin components flip sign when the propagation of light reverses. This correlation of the polarization and the propagation direction is named the spin-momentum locking (SML) [15]. For the ideal case, $|\mathbf{E}_{\perp}| = |\mathbf{E}_{\parallel}|$, the e-field is circularly polarized.

In order to characterize what degree the e-field is locked to the momentum or what percentage of circular polarization of the local light in the nanostructures, the circular polarization unit vectors are defined as

$$\hat{\sigma}^{\pm} = \frac{\hat{\mathbf{x}} \pm i\hat{\mathbf{y}}}{\sqrt{2}} , \quad (2)$$

where $\hat{\sigma}$ is for the right circularly polarized unit vector and $\hat{\sigma}^{-}$ for the left circularly polarized one and $\hat{\mathbf{x}}$ and $\hat{\mathbf{y}}$ are unit vectors along the x and y directions. Thus, the optical chirality (OC) of an e-field is defined as [17, 22]:

$$\mathcal{C} = \frac{|E(\mathbf{r}) \cdot \hat{\sigma}^{-}|^2 - |E(\mathbf{r}) \cdot \hat{\sigma}^{+}|^2}{|E(\mathbf{r})|^2} . \quad (3)$$

Obviously, the OC is limited to a region from -1 to 1 . Note that the value $\mathcal{C} = 1(-1)$ implies the e-field is entirely σ^- -(σ^+) polarized, while $\mathcal{C} = 0$ corresponds to a linear polarization. The intensity difference between the right circularly (σ^+) and the left circularly (σ^-) polarized components at the position r is calculated by $\mathcal{D} = |\mathbf{E}(\mathbf{r}) \cdot \hat{\sigma}^-|^2 - |\mathbf{E}(\mathbf{r}) \cdot \hat{\sigma}^+|^2$.

Then we focus on the interaction between the light possessing photonic SML and chiral quantum emitters with polarization-dependent dipole transitions. If a pair of counter-propagating spin-momentum-locked light interacts with quantum emitters, the interaction becomes chiral. In other words, the interaction strength for forward- and backward-propagating light modes is different. In this case, photon emission, absorption, and scattering become unidirectional. As a result, optical nonreciprocal flow of light can be achieved when a quantum emitter with degenerate transitions is populated in a specific spin state or one can shift the transition energy to make it couple (decouple) with one of the two of counter-propagating modes. On the basis of these effects, optical isolation can be realized at the single-photon level, which enables nonreciprocal single-photon devices, e.g., single-photon isolator and circulator. Next, we introduce the realization of single-photon isolators and circulators based on chiral light-matter interaction.

3. Single-photon isolation using chiral light-matter interaction

A single-photon isolator and circulator can be achieved by chirally coupling a quantum emitter to a passive, linear nanophotonic waveguide or a WGM microresonator which possesses optical chirality.

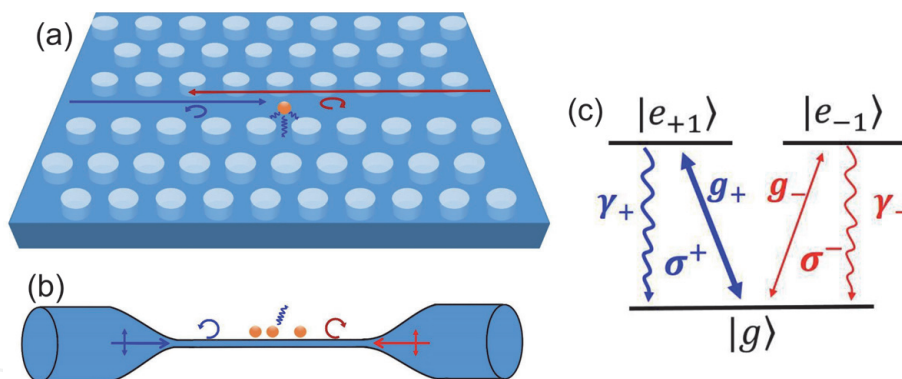
3.1 Single-photon isolator based on a nanophotonic waveguide

The type-I single-photon isolator is based on a line defect photonic crystal waveguide [16]. By carefully engineering the photonic crystal waveguide, it can have an in-plane circular polarization, and counter-propagating modes are counter circulating [22]. A quantum emitter is doped at the position where the waveguide possesses only the right-propagating σ^+ -polarized light or left-propagating σ^- -polarized light, as shown in **Figure 1a**. The doped emitter strongly interacts with the σ^+ -polarized light but weakly couples to the σ^- -polarized light. As a result, the time-reverse symmetry of the waveguide-emitter system breaks. The emitter scatters the forward- (right-) propagating single photons into an open environment whereas behaves transparently for the backward- (left-) propagating photons.

The steady-state transmission for the two atomic transitions coupling with waveguide is calculated by using the photon transport method [16, 23, 24]

$$t_{\pm}(\omega) = \frac{\omega - \omega_q - i(\gamma_{\pm} - \Gamma_{\pm})}{\omega - \omega_q + i(\gamma_{\pm} - \Gamma_{\pm})}, \quad (4)$$

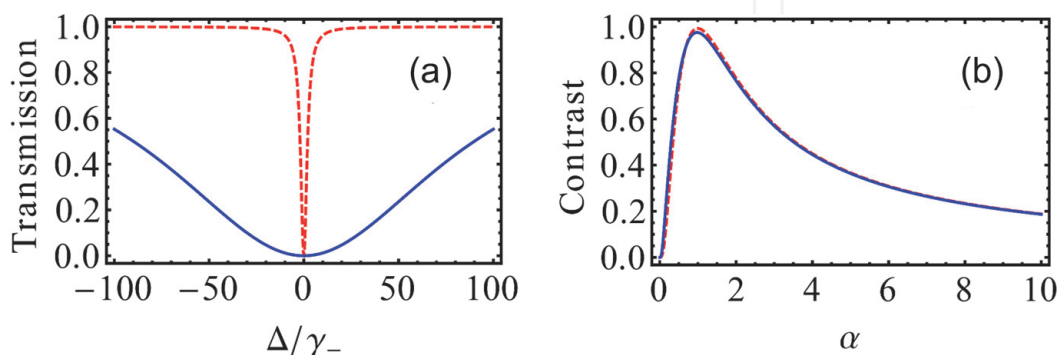
where ω is the frequency of the input photon and ω_q is the frequency of the atomic transition. The detuning is defined as $\Delta = \omega_q - \omega$. In $\Gamma_{\pm} = V_{\pm}^2/2v_g$, V_{\pm} is the coupling strength between the atom and the field in the waveguide, which is proportional to the atomic dipole moments μ_{\pm} , and v_g is the group velocity of the photon in the waveguide. A Cs atom is used as the quantum emitter so that $\mu_+ = \sqrt{45}\mu_-$, and γ_{\pm} , $\Gamma_{\pm} \propto |\mu_{\pm}|^2$. As a consequence, $\gamma_+/\gamma_- = \Gamma_+/\Gamma_- \gg 1$. The transmission is defined as $T_{\pm} = |t_{\pm}|^2$. The isolation contrast is evaluated as $\Upsilon = (T_+ - T_-)/(T_+ + T_-)$ [23].


Figure 1.

Schematics of the single-photon isolators. (a) Single-photon isolator based on a photonic crystal waveguide asymmetrically coupling with a quantum emitter. The waveguide possesses local circular polarization, and its rotating direction is dependent on the propagating direction [16]. The quantum emitter is doped in these specific sites. (b) Single-photon isolator based on a photonic nanofiber asymmetrically coupling with quantum emitters. The nanofiber is realized as the waist of a tapered silica fiber, whose evanescent fields exhibit propagation-direction-dependent circular polarization [18]. Quantum emitters are located in the vicinity of the nanofiber. (c) Energy-level diagram for a quantum emitter with unbalanced decay rates $\gamma_+ \gg \gamma_-$ and different coupling strengths with σ^\pm -polarized light $g_+ \gg g_-$. The states $|e_{\pm 1}\rangle$ and $|g\rangle$ correspond to excited states and a ground state, respectively, and the transition $|g\rangle \leftrightarrow |e_{+1}\rangle$ is driven by σ^+ -polarized light, while $|g\rangle \leftrightarrow |e_{-1}\rangle$ transition is driven by σ^- -polarized light. Here, quantum emitters can be Cs atoms [25], Rb atoms [26], or quantum dots [27].

Due to the coupling of the atom to the waveguide and open environment, the ratio of atomic dissipation rate is set to $\alpha = \Gamma_+/\gamma_+ = \Gamma_-/\gamma_-$. If $\alpha \approx 1$, the single-photon isolation is achieved, as shown in **Figure 2a**. Obviously, T_- is almost equal to unity for a right-hand input, while T_+ is small if $10 \leq |\Delta|/\gamma_- \leq 30$. Note that the transmissions are the same, ~ 0 at $\Delta = 0$ for both of the right-handed and left-handed inputs. At vanishing detuning, irrespective of the propagating direction, photons cannot be transmitted through the waveguide. However, the linewidths of the dips for the left-handed input (blue solid line) are much broader than those for the right-handed input (red dashed line). Because of this directionality-dependent linewidth, a single-photon wave packet with a duration $\Gamma_+^{-1} \ll \tau \ll \Gamma_-^{-1}$ when incident from the right is mostly transmitted through the waveguide, while when it is incident from the left, it is mostly scattered away to the open environment. Note that the performance of the single-photon isolation is dependent on the ratio α . As seen from **Figure 2b**, a good nonreciprocal behavior occurs only around the critical coupling $\alpha \approx 1$, and if $5\alpha \leq |\Delta|/\gamma_- \leq 10\alpha$ and $0.53 < \alpha < 1.8$, the isolation contrast Υ can be larger than 0.8.

Low-loss silica nanophotonic waveguides with a strongly nonreciprocal transmission controlled by the internal state of spin-polarized atoms have been


Figure 2.

(a) Steady-state transmission as a function of Δ for $\alpha = 1$. Solid blue curve is for transmission T_+ , and dashed red curve is for transmission T_- . (b) Isolation contrast as a function of α . Solid blue curve indicates Υ for $|\Delta|/\gamma_- = 10\alpha$ and dashed red curve for $|\Delta|/\gamma_- = 5\alpha$. The two curves are mostly overlapped. Figures are reproduced with permission from [16].

demonstrated [18]. In the experiment, an ensemble of individual cesium atoms is located in the vicinity of a subwavelength-diameter silica nanofiber (250-nm radius) trapped in a nanofiber-based two-color optical dipole trap [28]. As shown in **Figure 1b**, a quasilinearly polarized light incident to the nanofiber exhibits chiral character at the position of the atoms: when the evanescent field propagates in the forward direction, it is almost fully σ^+ -polarized, while it is almost fully σ^- -polarized if it propagates in the backward direction [18]. The experimental results show that the probe light with a power of 0.8 pW, corresponding to about 0.1 photon per excited-state lifetime, incident into nanofiber from different port obtains nonreciprocal transmissions, $T_+ = 0.13 \pm 0.01$ and $T_- = 0.78 \pm 0.02$, yielding an isolation $\mathcal{F} = 10|\log(T_-/T_+)| = 7.8$ dB [18]. Furthermore, trapping more atoms in the vicinity of the nanofiber can increase the isolation [18].

3.2 Single-photon isolator and circulator based on a WGM microresonator

The type-II single-photon isolator is based on a WGM microresonator. In this setup, when the linear polarized light enters the bus-waveguide from port P_1 , it excites a σ^+ -polarized counterclockwise (CCW) mode, while when it is incident from port P_2 , it drives σ^- -polarized clockwise (CW) mode [16]. As a result, the two counter-propagating modes in the WGM microresonator couple to a quantum emitter with different dipole moments μ_+ and μ_- corresponding to coupling strength g_+ and g_- .

The transmission into the bus and drop waveguides are calculated by [16].

$$t_{\pm,B}(\omega) = 1 + \frac{2i\kappa_{ex1}}{\omega_c - \omega - i\kappa - \frac{|g_{\pm}|^2}{\omega_q - \omega - i\gamma_{\pm}}}, \quad (5)$$

$$t_{\pm,D}(\omega) = \frac{2i\sqrt{\kappa_{ex1}\kappa_{ex2}}}{\omega_c - \omega - i\kappa - \frac{|g_{\pm}|^2}{\omega_q - \omega - i\gamma_{\pm}}}. \quad (6)$$

where $\kappa_{ex1(2)} = V_{1(2)}^2/2v_g$ is the decay rate of the resonator due to the external coupling $V_{1(2)}$ to the bus (drop) waveguide, and the photons in both of the bus and drop waveguides have the same group velocity v_g assumed. The total decay rate of the resonator is $\kappa = \kappa_i + \kappa_{ex1} + \kappa_{ex2}$ where κ_i is the intrinsic decay rate of the resonator. The detuning is defined as $\Delta = \omega_c - \omega$, and $\omega_c = \omega_q$ is assumed where ω_c is the resonating frequency of the resonator and ω_q is the transition frequency of the quantum emitter.

In the configuration of this device, if the drop waveguide is removed, i.e., $\kappa_{ex2} = 0$, single-photon isolator is achieved (see **Figure 3**). In this case, $T_{\pm,B}$ is substituted with T_{\pm} . As shown in **Figure 4**, if $g_- = 0$ and $g_+ \gg \kappa_i$, at $\Delta = 0$, $T_+ = 1$, while $T_- \approx 0$. This can be achieved by using a negatively charged quantum dot as the quantum emitter [27]. If $|g_-| > 0$ and $\Delta \approx 0$, the nonreciprocal window disappears. However, when $|\Delta| \approx |g_-|$, $\gamma_+ = 0$, and $g_+/\kappa_i \gg 1$, the right-moving photon can pass through the device, corresponding to $T_+ = 1$ (solid blue curve), while the left-moving photon decays into the environment via the resonator, corresponding to $T_- = 0$ (solid red curve). At $|\Delta| \approx |g_+|$, the optical nonreciprocity is reversed. The device is transparent for left-moving photon but blocks the right-moving photon. If $\gamma_+ \gg \kappa_i$, the part of the excitation of the right-moving photon can pass through the device (dotted green curve).

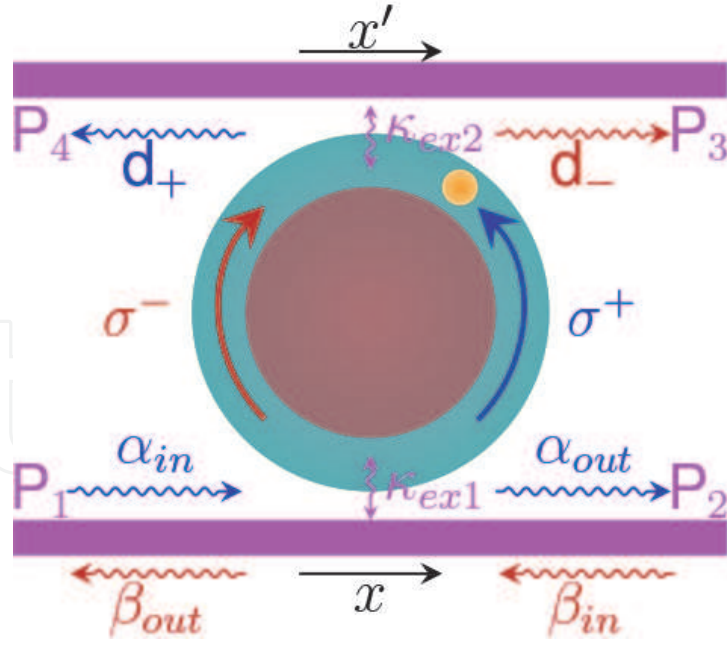


Figure 3. Schematic of the single-photon isolator or circulator. There is a quantum emitter doped in a WGM microresonator, which possesses a σ^+ -polarized CCW mode and a σ^- -polarized CW mode. The microresonator couples to a lower bus waveguide with a rate κ_{ex1} and a upper drop waveguide with a rate κ_{ex2} . Reproduced with permission from [16].

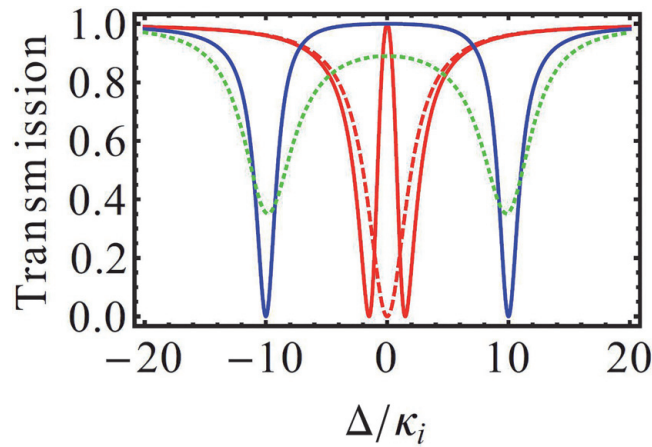


Figure 4. Steady-state transmissions of the single-photon isolator using a WGM microresonator in the absence of the drop waveguide, i.e., $\kappa_{ex2} = 0$, and under the critical coupling condition $\kappa_{ex1} = \kappa_i$. Dashed and solid curves are for the transmission T_- when $g_- = 0$ and $g_- = g_+/\sqrt{45}$, while solid blue and dotted green curves are for the transmission T_+ when $\gamma_+ = 0$ and $\gamma_+ = 3\kappa_i$, respectively. $g_+ = 10\kappa_i$. Reproduced with permission from [16].

A WGM bottle microresonator coupling to the optical fiber and a single ^{85}Rb atom to realize the type-II optical isolator has been demonstrated [18]. In the experiment, for the bottle microresonator, it sustains WGMs with ultrahigh quality factor and small mode volume [26]. As a result of strong transverse confinement, its evanescent fields of WGMs are almost fully circularly polarized, with OC $\mathcal{C} > 0.96$ [26]. The single ^{85}Rb atom is prepared in the outermost $m_F = 3$ Zeeman substate of the $F = 3$ hyperfine ground state. As seen from **Figure 1c**, the states $|e_{+1}\rangle$ and $|e_{-1}\rangle$ correspond to the excited states $|F' = 4, m_{F'} = +4\rangle$ and $|F' = 4, m_{F'} = +2\rangle$, respectively. In the experiment, the transition $|g\rangle \rightarrow |e_{+1}\rangle$ is much stronger than the $|g\rangle \rightarrow |e_{-1}\rangle$ transition, corresponding to the coupling strength, g_+ and g_- , between the atom and the two counterrotating WGMs, yielding $g_+/g_- = 5.8$ [18]. The experimental results show that when the probe light with power of 3 pW, corresponding

to about 0.2 photon per resonator lifetime, obtains nonreciprocal transmissions through the system of $T_+ = 0.72 \pm 0.02$ in the forward direction and $T_- = 0.03 \pm 0.01$ in the backward direction, yielding an isolation $\mathcal{F} = 13$ dB.

The single-photon circulator consists of two waveguides and a WGM microresonator, and both of the bus and drop waveguides overcouple to the resonator, i.e., $\kappa_{ex1} = \kappa_{ex2} = 3\kappa_i$ (see **Figure 3**). As seen from **Figure 5a**, at $\Delta \sim 0$, for port P_1 input α_{in} , most excitation of the photon can transport to the bus-waveguide port P_2 , $T_{+,B} = 0.85$ (solid blue curve), while the output to the drop-waveguide port P_4 is vanishingly small (dashed blue curve). As for port P_2 input β_{in} , there is a dip (peak) in the transmission $T_{-,D}$ ($T_{-,B}$), but the linewidth is very small, $\sim 0.16\kappa_i$, as shown in **Figure 5a**. In contrast, the whole transmission spectrum has a linewidth of $11\kappa_i$. As a result, a single-photon pulse bandwidth $0.16\kappa_i \ll \Delta B \ll 11\kappa_i$ can transport to the drop-waveguide port P_3 with a probability of 0.74. The probability of transmitting to the bus-waveguide port P_1 is small, ~ 0.02 , yielding a contrast 0.95. The numerical simulations of the propagation of a single-photon pulse are performed in [16], which match the analytic forms well (see gray curves in **Figure 5a**). If $|\Delta| \sim g_-$, $T_{+,B} = 0.835$ to the P_2 , $T_{+,D} = 0.032$ to P_4 , and $T_{-,B} = 0.021$ to the P_1 , $T_{-,D} = 0.733$ to P_3 . As a consequence, the device forms a $P_1 \rightarrow P_2 \rightarrow P_3$ circulator. The single-photon incident from port P_1 transmits to port P_2 , but the photon entering port P_2 comes out from port P_3 .

If $\Delta \sim 0$, the numerical simulations of the propagation of a single-photon pulse in time as it passed through the circulator are performed in [16]. **Figure 5b** shows Gaussian pulse wave packets, $\phi(x, 0)_{\pm,B} = \sqrt{4\tau^2/\pi} e^{-(x-x_0)^2/2\tau^2}$, incident from port P_1 and P_2 at the same time t_d . The transmissions are calculated by $T_{\pm,B/D} = \int_{-\infty}^{+\infty} \phi_{\pm,B/D}^*(x, t_d) \phi(x, t_d) dx$ to be $\{T_{+,B}, T_{-,B}, T_{+,D}, T_{-,D}\} = \{0.9, 0.178, 0.02, 0.675\}$ excitations output to port $\{P_2, P_1, P_4, P_3\}$. Obviously, a three-port circulator at the single-photon level is achieved.

Note that if the states are initially populated to $|6^2S_{1/2}, F = 4, m = -4\rangle$ for Cs atoms or $|5^2S_{1/2}, F = 3, m = -3\rangle$ for Rb atoms, $\mu_+ \ll \mu_-$, the optical nonreciprocity can be reversed, and the single-photon circulator forms a $P_2 \rightarrow P_1 \rightarrow P_4$ circulator.

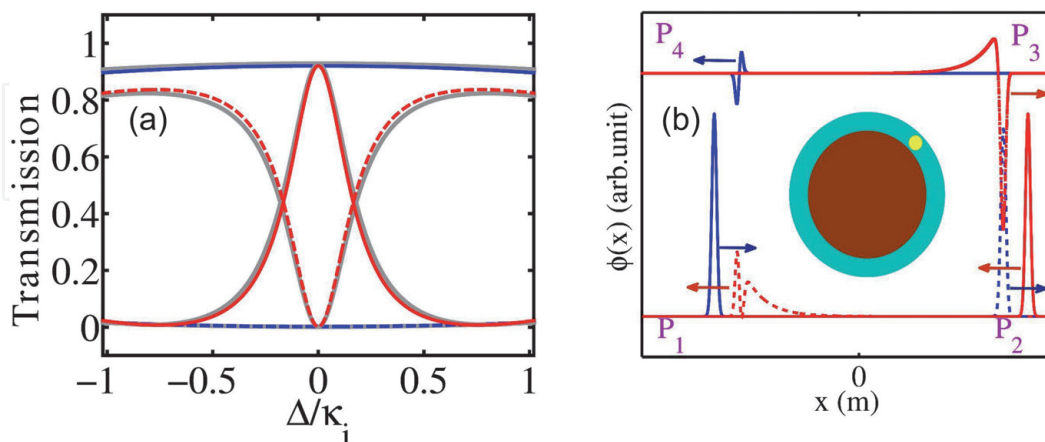


Figure 5. (a) Steady-state transmissions of the single-photon circulator using a WGM microresonator and both of the bus and drop waveguides overcouple to the resonator, i.e., $\kappa_{ex1} = \kappa_{ex2} = 3\kappa_i$. Solid blue (red) curve is for the transmission $T_{+,B}$ ($T_{-,B}$) in the bus waveguide, while the dashed blue (red) curve is for the transmission $T_{+,D}$ ($T_{-,D}$) in the drop waveguide. The gray curves are the results from numerical simulations, which mostly overlap with other curves. $g_+ = 5\kappa_i$, $g_- = g_+/\sqrt{45}$, $\gamma_+ = 0.3\kappa_i$, and $\gamma_- = \gamma_+/45$. (b) Propagation of single-photon pulses with $\sim 4\kappa_i$ in the resonator for $\Delta = 0$ and $v_g = 1 \times 10^8$ m/s. Blue (red) lines are for the input and transmitted excitations for the left-handed (right-handed) input. The arrows indicate the moving directions of photons. Reproduced with permission from [16].

A quantum optical circulator operated by a single atom has been demonstrated [19]. In the experiment, a single ^{85}Rb atom is coupled to the WGM of a bottle microresonator, which is interfaced by two tapered fiber couplers, realizing a four-port device. The single ^{85}Rb atom is prepared in the outermost Zeeman sublevel $m_F = +3$ of the $5S_{1/2}$, $F = 3$ hyperfine ground state. The light in the CCW mode excites state $|F' = 4, m_{F'} = +4\rangle$ more strongly than CW mode exciting $|F' = 4, m_{F'} = +2\rangle$ state, corresponding to coupling strength of resonator modes and the atom, $g_+ \gg g_-$. The presence of the atom changes the resonator field decay rate from $\kappa_{\text{tot}} = \kappa_i + \kappa_{\text{ex}1} + \kappa_{\text{ex}2}$ to $\kappa_{\text{tot}} + \Gamma_{\pm}$, where $\Gamma_{\pm} = g_{\pm}^2/\gamma$ is the direction-dependent atom-induced loss rate [19] and $\gamma = 2\pi \times 3$ MHz is the dipole decay rate of Rb. For the CW mode, Γ_- is small, and the resonator field decay rate is not substantially modified by the atom, whereas for the CCW mode, Γ_+ can become comparable with or even exceed κ_{tot} . As a result, when light is incident into the device from ports P_2 and P_4 for which it couples to the CW mode (see **Figure 3**), the add-drop functionality is achieved. However, for the two other input ports P_1 and P_3 , the light couples to the CCW mode, and the incident light field remains in its initial fiber in the condition of the resonator-atom system operating in the undercoupled regime, $\kappa_{\text{ex}1}, \kappa_{\text{ex}2} \ll \Gamma_+$. Overall, the device realizes an optical circulator that routes light from the input port P_i to the adjacent output port P_{i+1} with $i \in \{1, 2, 3, 4\}$ (see **Figure 3**).

In the experiment, the transmissions T_{ij} to all output ports P_j when sending a weak coherent probe field into the four different input ports P_i have been measured [19]. And the performance of the circulator can be quantified with the fidelity \mathcal{F} and the average photon survival probability η . The fidelity is evaluated as the overlap of the renormalized transmission matrix $\tilde{T} = (T_{ij}/\eta_i)$ with the one expected for the ideal circulator, T^{id} . Here, $\eta_i = \sum_k T_{i,k}$ is the survival probability of a photon entering port P_i . Thus, the average operation fidelity of the circulator is [19]

$$\mathcal{F} = \frac{\text{Tr}[\tilde{T}T^{\text{id},T}]}{\text{Tr}[T^{\text{id}}T^{\text{id},T}]}, \quad (7)$$

giving the probability of the correct circulator operation average over various inputs. The minimum fidelity is $\mathcal{F} = 0$, whereas $\mathcal{F} = 1$ is reached for ideal operation. The experimental results show an optimum circulator performance for $\kappa_{\text{tot}}/2\kappa_i = 2.2$, where $\mathcal{F} = 0.72 \pm 0.03$ and, at the same time, $\eta = 0.73 \pm 0.04$.

Furthermore, the circulator performance can also be quantified by the isolations [19].

$$I_i = 10 \log (T_{i,i+1}/T_{i+1,i}) . \quad (8)$$

For the optimum working point, it achieves $\{I_i\} = \{10.9 \pm 2.5, 6.8 \pm 1.3, 4.7 \pm 0.7, 5.4 \pm 1.1\}$ dB and an average insertion loss of $-10 \log \eta = 1.4$ dB [19].

Note that when the atom is prepared in the opposite Zeeman ground state, $F = 3, m_F = -3$, the operation direction of the circulator is reversed.

The type-III single-photon isolator is based on a microring resonator coupling to a QD and a nearby waveguide [17]. In the approach, the silicon microring resonator in which light is tightly transversely confined has an exceptionally strong evanescent e-field and a near-unity OC surrounding the whole outside and inside walls of the resonator. By initializing a quantum dot (QD) in a specific spin ground state or using the optical Stark control, a broadband single-photon isolation over several gigahertz is achieved.

The QD-resonator system consists of a silicon waveguide, a silicon microring resonator, and a single negatively charged quantum dot (QD). Numerical

simulations using the finite-difference time-domain (FDTD) method are performed to calculate the properties of the resonator. At the resonant wavelength $\lambda_c \sim 1.556 \mu\text{m}$, the intrinsic quality factor Q_{in} is about 3.9×10^4 , and the mode volume V_m is about $1.55 \mu\text{m}^3$. The corresponding resonance frequency and the intrinsic decay rate are $\omega_c/2\pi \approx 192.67 \text{ THz}$ and $\kappa_i/2\pi \approx 4.94 \text{ GHz}$, respectively, yielding a total decay rate of $\kappa = \kappa_{ex} + \kappa_i \approx 2\pi \times 9.88 \text{ GHz}$, where WGMs decay into the waveguide at the rate κ_{ex} and $\kappa_{ex} = \kappa_i$ at resonance.

When the light enters the waveguide from port $P_1(P_2)$ with transverse electric mode and excites the CCW (CW) WGMs, the evanescent fields of interest circulating around the sidewalls of the resonator are tightly confined in the transverse direction as a transverse magnetic mode. The e-field distribution and the OC of the microring resonator are numerically investigated by FDTD simulation. For a TE mode incident to port $P_1(P_2)$, the intensity difference \mathcal{D} is shown in **Figure 6a–c**. When the light enters the waveguide from port P_1 , the outer (inner) evanescent field of the WGM is σ^+ (σ^-) polarized, indicated by $\mathcal{C} \approx -1(1)$, as shown in **Figure 6b**. For the light incident to port P_2 , the polarization of the evanescent field is reversed, as shown in **Figure 6d**. Note that in this resonator, $|\mathcal{C}| > 0.99$ from the surface of the outside wall to a position 280 nm away in the radial direction [17]. This large chiral area greatly relaxes the requirement for precisely positioning a QD. Importantly, the intensities of the evanescent fields near the outside wall are almost equal to that in the middle of the resonator, and they are still strong even at a position tens of nanometers away from the surface. These

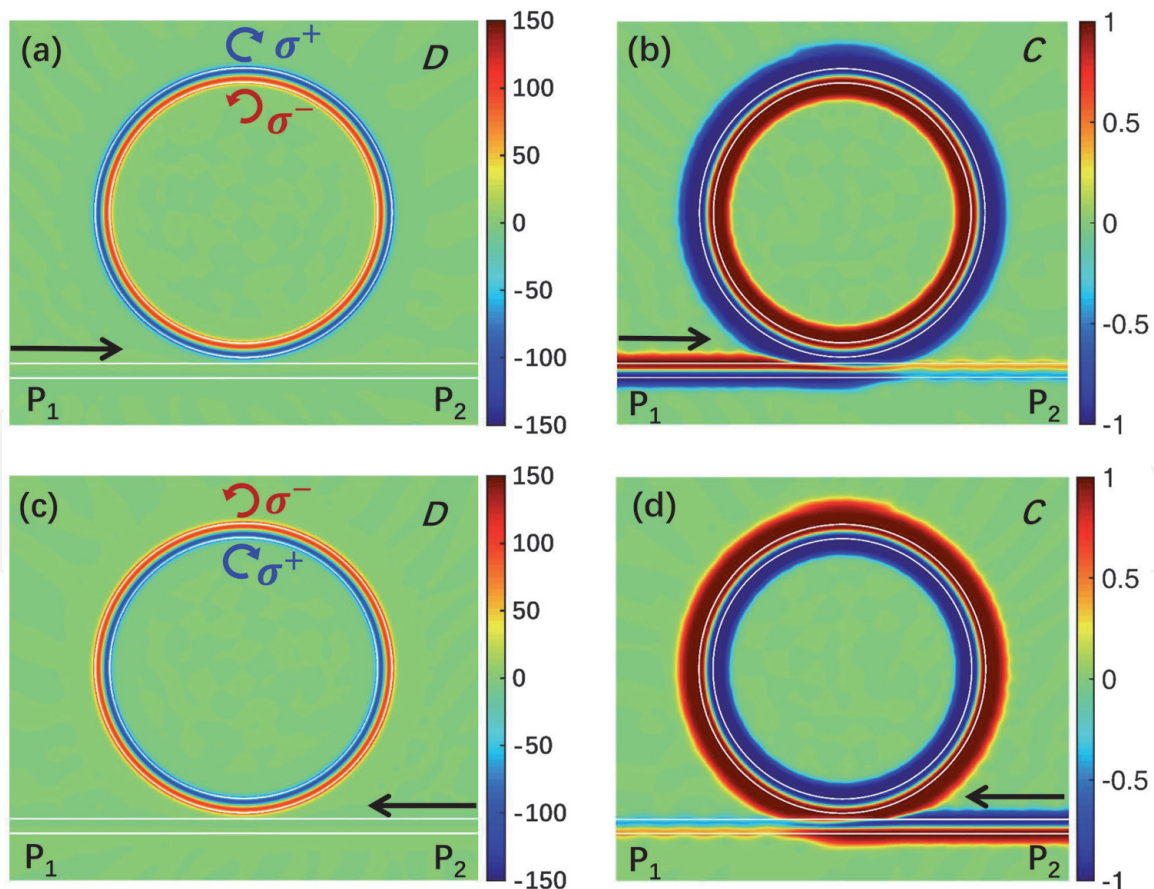


Figure 6. (a, c) Intensity difference \mathcal{D} and (b, d) optical chirality \mathcal{C} for light with $\lambda = 1.556 \mu\text{m}$. Here, to clearly show the chiral e-fields in the vicinity of the resonator and wipe off the negligibly weak background, we use the definition for $\mathcal{C} = \left(|\mathbf{E}(\mathbf{r}) \cdot \hat{\sigma}^-|^2 - |\mathbf{E}(\mathbf{r}) \cdot \hat{\sigma}^+|^2 \right) / \left(|\mathbf{E}(\mathbf{r})|^2 + q \right)$, where we introduce a small bias, $q = \max \{ |\mathbf{E}(\mathbf{r})|^2 \} \times 10^{-4}$, in the denominator. Light incident to port P_1 (a, b) and port P_2 (c, d). White lines are for the waveguide boundaries. Reproduced with permission from [17].

features of the resonator allow a strong chiral coupling between a nearby QD and the resonator.

As seen in **Figure 7**, a negatively charged QD is doped near the outside wall of the resonator. It has two energy-degenerate transitions at $\lambda_q \sim 1.556 \mu\text{m}$, driven by a circularly polarized e-field, as seen in **Figure 8a**. It can be an InAs self-assembled QD grown on silicon dioxide/silicon substrates [29], with two electronic spin ground states $|\pm 1/2\rangle$ and two optically excited states $|\pm 3/2\rangle$.

By initializing the QD in a specific spin ground state or shifting the transition energy with the optical Stark effect (OSE), chiral QD-resonator interaction can be achieved. As shown in **Figure 8b**, by applying a magnetic field along the direction perpendicular to the growth direction of the QD, the spin-flip Raman transitions are enabled and can couple to linearly polarized e-fields. In this case, the spin ground state $|1/2\rangle$ or $|-1/2\rangle$ can be selectively prepared with a near-unity possibility [27, 30]. When the spin ground state, e.g., $|1/2\rangle$, is populated and the magnetic field is switched off, the QD can be treated as a two-level system with a dipole moment coupling only with a σ^+ -polarized e-field, as shown in **Figure 8c**. The second method involves all-optical control of the QD via the optical Stark control. The polarization-selective transition, $|1/2\rangle \leftrightarrow |3/2\rangle$ or $|-1/2\rangle \leftrightarrow |-3/2\rangle$, can also be tuned to have different energies by inducing a large optical Stark shift with a large detuned circularly polarized light [31, 32]. As shown in **Figure 8d**, the σ^+ -polarized transition is shifted by σ^+ -polarized classical light to be on resonance with the CCW mode, while the σ^- -polarized transition of the QD decouples to the resonator due to a large detuning $\Delta_- = \Delta_c + 2\Delta_{OSE}$, where Δ_c is the detuning of resonator's resonance and Δ_{OSE} is the detuning which resulted from the OSE. In this case, the QD can also be treated as a two-level system with a σ^+ -polarized transition.

After QD spin ground state preparation, the QD strongly couples to the CCW mode with large strength g_+ but decouples from the CW mode with a much smaller strength g_- . Note that the OSE-based method allows an all-optical operation. In fabrication, the QD can be engineered to have various resonance wavelengths, dipole moments, and decoherence rates. Self-assembled quantum dots can be engineered to possess a transition at $1.556 \mu\text{m}$, and their dipole moment can vary

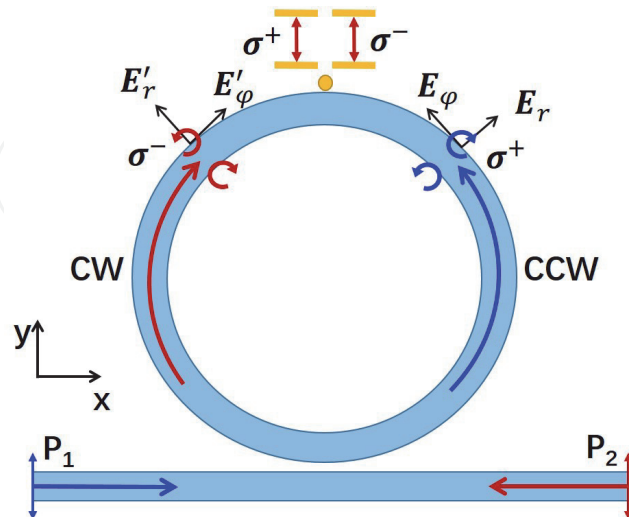


Figure 7.

Schematic of the single-photon isolation based on a microring resonator. The silicon resonator couples to a nearby silicon waveguide with refractive index $n = 3.48$ and a single negatively charged QD. The resonator and the waveguide are $0.44 \mu\text{m}$ wide and $0.22 \mu\text{m}$ thick. The resonator has a $4.22 \mu\text{m}$ radius. The light incident to port P_1 (P_2) drives the counterclockwise (CCW) [clockwise (CW)] WGM. The polarization of the evanescent field of the CCW mode is σ^+ - (σ^- -) polarized near the whole outside (inside) wall, while that for the CW mode is σ^- - (σ^+ -) polarized. After initialization for the QD, it is treated as a two-level system with σ^+ -polarized transition. Reproduced with permission from [17].

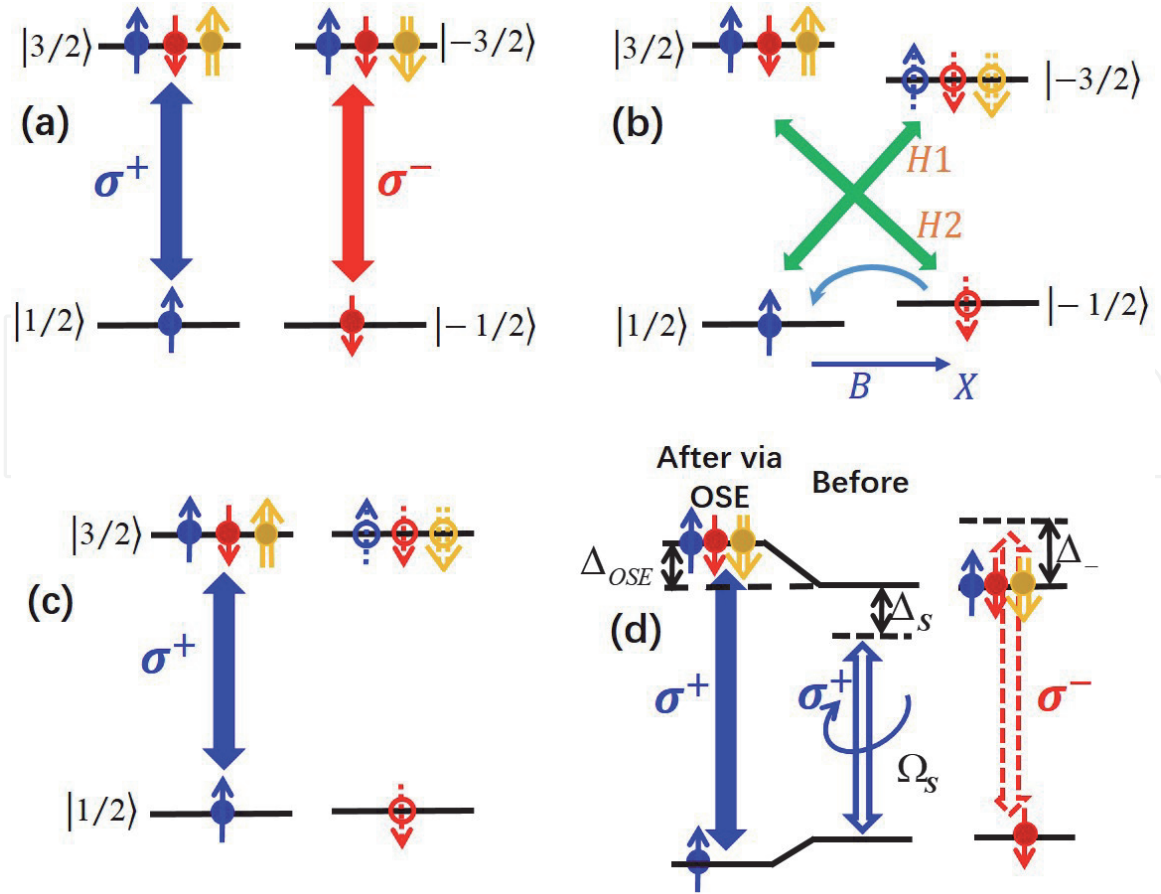


Figure 8. Initialization of a negatively charged QD including two methods: Coherent population trapping (a–c) and optical Stark effect (d). (a) Four-level configuration of an electron spin in a single negatively charged QD. (b) Four-level configuration with dipole-allowed transitions, enabled by a magnetic field along the X direction. (c) The Trion system which has been pumped with linearly polarized light at the magnetic field can be treated as a two-level system only with σ^+ -polarized light excitation at zero magnetic field. (d) A σ^+ -polarized classical light Ω_s with a detuning Δ_s from the σ^+ -polarized transition $|1/2\rangle \leftrightarrow |3/2\rangle$ is applied to shift the transition energy by $\Delta_{OSE} \propto \Omega_s^2 / \Delta_s$. The σ^- -polarized CW mode decouples from the QD because it is detuned by Δ_- from the relevant transition $|-1/2\rangle \leftrightarrow |-3/2\rangle$. Figures are reproduced with permission from [17] and are slightly modified.

from a few Debye to 40 Debye [33]. Here, we choose the resonance wavelength $\lambda_q \approx 1.556 \mu\text{m}$, $\omega_q = \omega_c$, and the dipole moment $|\mathbf{d}| = 30$ Debye, yielding a spontaneous emission rate $\gamma_q = |\mathbf{d}|^2 \omega_q^2 / 3\pi\epsilon_0 \hbar c^3 = 2\pi \times 11.88$ MHz. The strength of the zero-point fluctuation of this mode is $|\mathbf{E}_0| = \sqrt{\hbar\omega_c / (2\epsilon_0 V_m)} \approx 6.82 \times 10^4$ V/m, where ϵ_0 is the vacuum permittivity and \hbar is the Planck constant. Correspondingly, the QD-resonator coupling strength $g = \mathbf{d} \cdot \mathbf{E}_0 / \hbar \approx 2\pi \times 10.29$ GHz. And asymmetry coupling strength $|g_+| = \alpha g$ and $|g_-| = \beta g$, where $\alpha = \sqrt{(1-C)/2}$ and $\beta = \sqrt{(1+C)/2}$ [17]. As a consequence, the QD-resonator system is chiral and subsequently achieves the optical isolator at the single-photon level.

The steady-state forward (backward) transition amplitude t_+ (t_-), corresponding to the left-handed (right-handed) input, is derived by using the single-photon scattering method [17, 24, 34]

$$t_+ = \frac{\tilde{\Delta}_c [\tilde{\Delta}_c \tilde{\Delta}_q - G^2] + \tilde{\Delta}_q \kappa_{ex}^2 - g_+^* g_- h - g_+ g_-^* h^* - \tilde{\Delta}_q |h|^2 + i(|g_-|^2 - |g_+|^2) \kappa_{ex}}{(\tilde{\Delta}_c + i\kappa_{ex}) [\tilde{\Delta}_q (\tilde{\Delta}_c + i\kappa_{ex}) - G^2] - g_+^* g_- h - g_+ g_-^* h^* - \tilde{\Delta}_q |h|^2}, \quad (9)$$

$$t_{-} = \frac{\tilde{\Delta}_c [\tilde{\Delta}_c \tilde{\Delta}_q - G^2] + \tilde{\Delta}_q \kappa_{ex}^2 - g_{-}^* g_{+} h - g_{-} g_{+}^* h^* - \tilde{\Delta}_q |h|^2 + i(|g_{+}|^2 - |g_{-}|^2) \kappa_{ex}}{(\tilde{\Delta}_c + i\kappa_{ex}) [\tilde{\Delta}_q (\tilde{\Delta}_c + i\kappa_{ex}) - G^2] - g_{-}^* g_{+} h - g_{-} g_{+}^* h^* - \tilde{\Delta}_q |h|^2}, \quad (10)$$

where $\tilde{\Delta}_c = \omega - \omega_c + i\kappa_i$, $\tilde{\Delta}_q = \omega - \omega_q + i\gamma_q$, and $G^2 = |g_{+}|^2 + |g_{-}|^2$. The detuning is defined as $\Delta_c = \omega - \omega_c$ and $\omega_c = \omega_q$ is assumed. In this device, $|C| = 0.99$ and $|h| \ll \kappa_i$, the transmissions, $T_{\pm} = |t_{\pm}|^2$, are shown in **Figure 9**. In the absence of the backscattering, i.e., $h = 0$, at $\Delta_c = 0$, $T_{+} \approx 0.99$ and $T_{-} \approx 0$, yielding the insertion loss of $\mathcal{L} = -10 \log(T_{+}) \approx 0.04$ dB and the isolation contrast $\Upsilon \approx 1$. Consequently, at vanishing detuning, the single-photon isolation is achieved with almost zero insert loss and near-unity isolation contrast. The nonreciprocal bandwidth is about $1.3\kappa \approx 2\pi \times 12.8$ GHz, which is about two to three orders broader than those in [16, 18–20, 35]. It can be seen from **Figure 9a** that the nonreciprocal spectral window becomes narrower and narrower as the backscattering strength increases; for a relatively large backscattering $|h| = \kappa_i$, both the backward and forward transmissions only change very slightly, but for an extremely large backscattering $|h| = 3\kappa_i$, the nonreciprocal performance is much affected. As shown in **Figure 9b**, in the absence of backscattering, the isolation contrast is quite robust, decreasing slowly from 1 to 0.8 as the OC changes from -1 to -0.5 (blue solid curve), while the insertion loss increases almost linearly in this region.

This device can achieve optical isolation when oppositely propagating photons enter the system at the same time, avoiding the dynamic reciprocity problem [36].

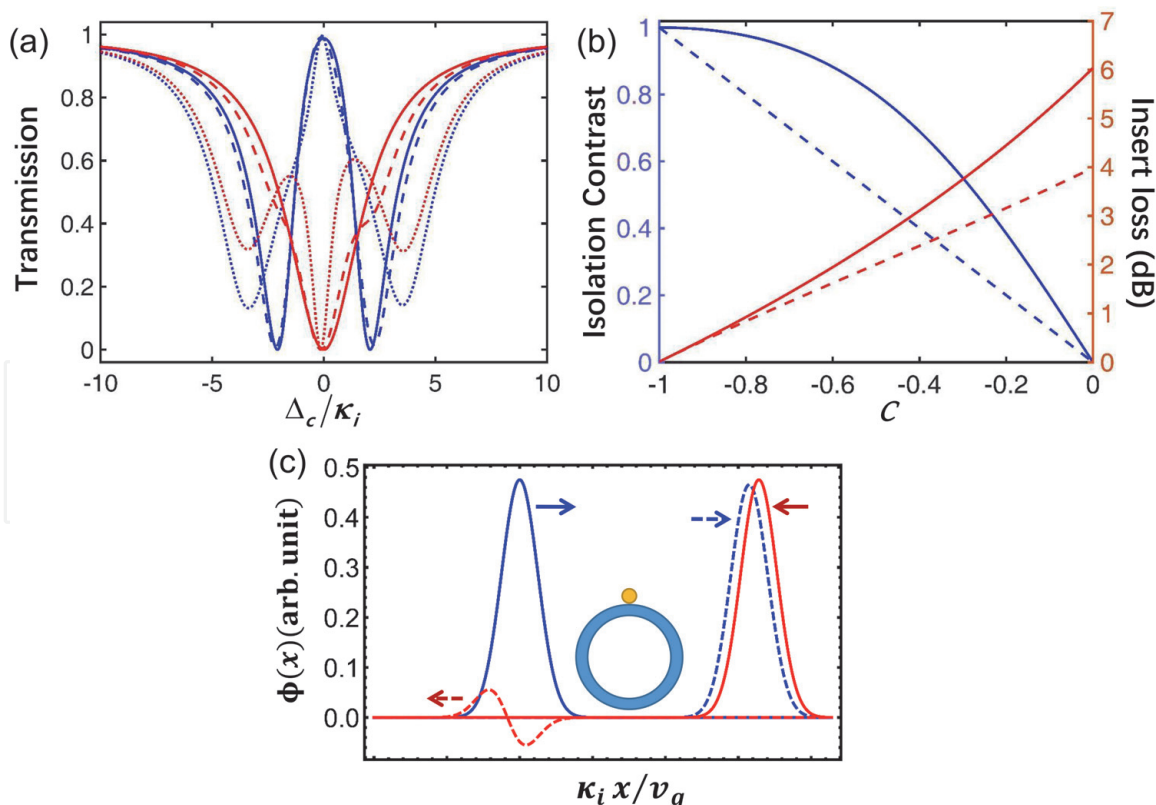


Figure 9.

(a) Steady-state transmissions for $|D| = 0.99$. Blue (red) curves are for transmissions T_+ (T_-), $h = 0$ (solid curves) for $|h| = \kappa_i$ (dashed curves), and $|h| = 3\kappa_i$ (dotted curves). (b) Blue curve is for isolation contrast, and red dashed curve is for insert loss as a function of the optical chirality D for $h = 0$ (solid curves) and $|h| = \kappa_i$ (dashed curves). (c) Propagation of single-photon pulses incident to ports P_1 and P_2 simultaneously. Red thin (blue thick) curves are for the propagation of the right-moving (left-moving) single-photon pulses. Solid curves are for incident single-photon wave function, and dashed curves are for transmitted wave function. $|D| = 1$ for simplicity.

Numerical simulations for the propagation of single-photon wave packets incident to ports P_1 and P_2 simultaneously are performed by using wave-vector-space method [17]. The propagation of single-photon pulses in the system is shown in **Figure 9c**. At resonance, a right-moving single photon can pass through the system with transmission probability 0.98, while that of a left-moving single photon is only 0.02.

4. Optical isolation via chiral cross-Kerr nonlinearity

In a waveguide embedded with N -type atoms (see the upper waveguide in **Figure 10a**), the classical switching and coupling fields are applied to induce the phase shift ϕ and amplitude modulation ξ of the probe field. The forward and backward amplitude transmissions ξ_f and ξ_b are sufficiently different after the probe field passes through the ensemble of atoms. Thus, the type-IV optical isolator is achieved.

Rb atoms are used to create the chiral XKerr nonlinearity. In the $|2\rangle \rightarrow |1\rangle$ transition, the $|2\rangle \rightarrow |3\rangle$ transition, and $|4\rangle \rightarrow |3\rangle$ transition of the Rb atoms with decay rates γ_{21} , γ_{22} , and γ_{43} , respectively, $\gamma_{21} = \gamma_{23} = \gamma_{43} = \gamma_0$ is assumed, and $\gamma_0 \gg \Gamma$, where Γ is the dephasing rates of both ground states $|1\rangle$ and $|3\rangle$ and $\gamma_0 = 2\pi \times 6$ MHz. The XKerr nonlinearity can be efficiently induced between the probe and switching fields in the configuration and can be modified by the coupling laser. As shown in **Figure 10b**, the switching (coupling, probe) field drives the transition $|1\rangle \leftrightarrow |2\rangle$ ($|3\rangle \leftrightarrow |2\rangle$, $|3\rangle \leftrightarrow |4\rangle$) with a detuning Δ_s (Δ_c , Δ_p) in the absence of

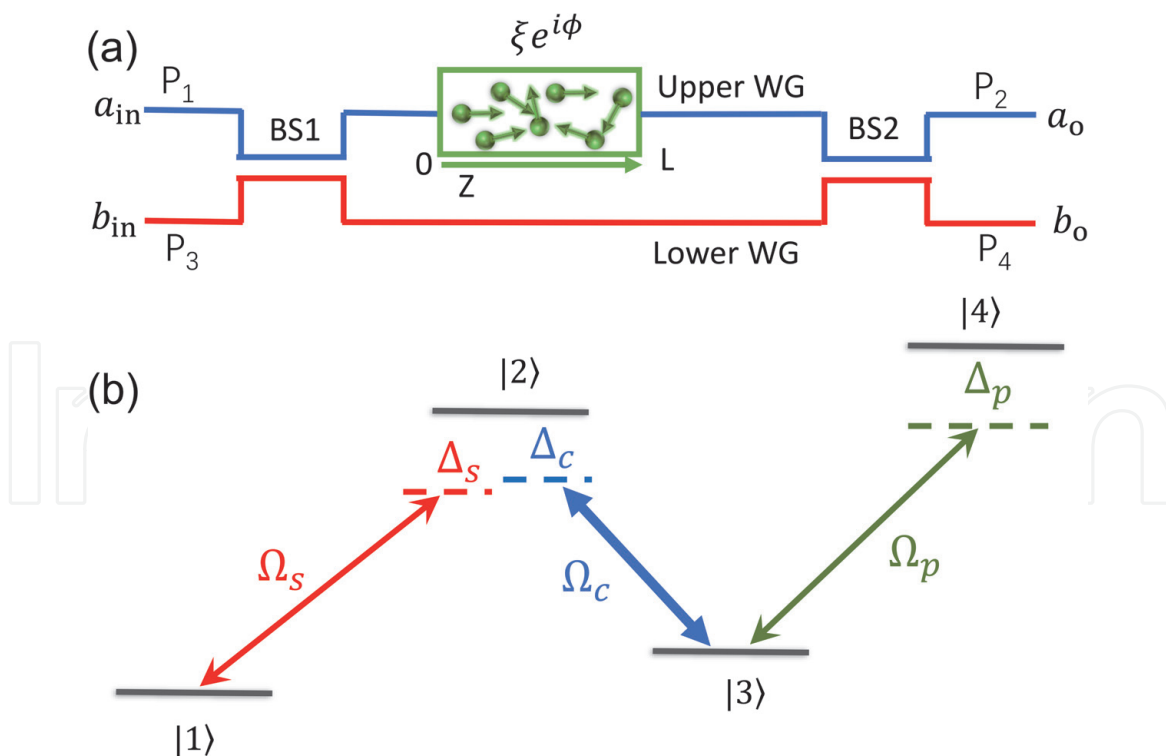


Figure 10. (a) Schematic of the realization of optical isolator and circulator by using chiral cross-Kerr nonlinearity. To realize an optical isolator, we use only the upper waveguide (WG) embedded with a cloud of N -type atoms. The photon passing through the atoms suffers an amplitude transmission of ξ and a phase shift ϕ , which are dependent on its propagation direction. To achieve optical circulator, the lower waveguide is added to form a Mach-Zehnder interferometer with the upper one by using two beam splitters BS1 and BS2. (b) Energy-level diagram of N -type atoms. The switching (carrier frequency Ω_s), coupling (Ω_c), and probe (Ω_p) fields couple to transition $|1\rangle \leftrightarrow |2\rangle$, $|3\rangle \leftrightarrow |2\rangle$, and $|3\rangle \leftrightarrow |4\rangle$, with detunings Δ_s , Δ_c , and Δ_p , respectively. Reproduced with permission from [20].

thermal motion. The switching (coupling, probe) laser beam has the carrier frequency Ω_s (Ω_c , Ω_p), corresponding to the wave vector k_s (k_c , k_p). At room temperature, the inevitable random thermal motion of the j th atom moving with velocity v_j induces the “microscopic” Doppler shifts $k_s v_j$, $k_c v_j$, and $k_p v_j$ in the corresponding atomic transitions, respectively. The strength of the nonlinearity is strongly dependent on the effective detunings, and thus the Doppler shifts. As a result, these frequency shifts change the optical nonlinearity in a way strongly dependent on the propagation direction of the probe field with respect to the switching and coupling fields, leading to the chiral XKerr nonlinearity. Both the switching and coupling laser beams are left-moving and $k_s v_j = k_c v_j$ is assumed. Thus, the backward-moving (forward-moving) probe field “sees” the same (opposite) Doppler shift as the switching and coupling ones. Compared with the backward input case, where the Doppler broadening significantly reduces the total XKerr nonlinearity, the Doppler shift “seen” by the forward-moving probe field is partly compensated, and subsequently the nonlinearity remains large [20].

For a centimeter-scale medium, e.g., $L = 2$ cm, the medium is absorptive, and the forward and backward transmissions are very different, as shown in **Figure 11a**. As the probe detuning increases, the forward transmission T_{12} rapidly increases to 0.80 at $\Delta_p = 35.6\gamma_0$, corresponding to an insertion loss of 1 dB. As a result of Doppler broadening, the backward transmission T_{21} is much smaller than T_{12} , when $35.6\gamma_0 < \Delta_p < 60.6\gamma_0$. In this region, the insertion loss is smaller than 1 dB, while the isolation ratio is larger than 15 dB. The isolation ratio can be considerably improved with a large forward transmission by using a longer medium or, equivalently, increasing the density of the atoms. For $L = 4$ cm, the isolation rate can reach more than 30 dB in the range of $50\gamma_0 < \Delta_p < 60\gamma_0$, yielding an isolation bandwidth of $2\pi \times 60$ MHz. At the same time, the insertion loss is less than 1 dB. As a consequence, an isolation can be achieved by using this medium.

By carefully choosing the density and length of the atomic vapor, and properly arranging the switching and coupling fields, a phase shift difference, $\Delta\phi = \phi_f - \phi_b$, can approach π with high transmissions ξ_f and ξ_b . It can realize a four-port optical circulator by adding a lower waveguide to form a Mach-Zehnder interferometer (MZI), as seen in **Figure 10a**.

For a short medium ($L = 3.33$ mm), the transmission of the forward- and backward-moving probes can be comparably high, but the phase shift ϕ_b is always small, specifically about 0.011π at $\Delta_p = 7.77\gamma_0$, as shown in **Figure 11b**. In contrast, at the optimal point $\Delta_p^{\text{opt}} = 7.77\gamma_0$, the difference of the phase shift, $\phi_f - \phi_b$, reaches

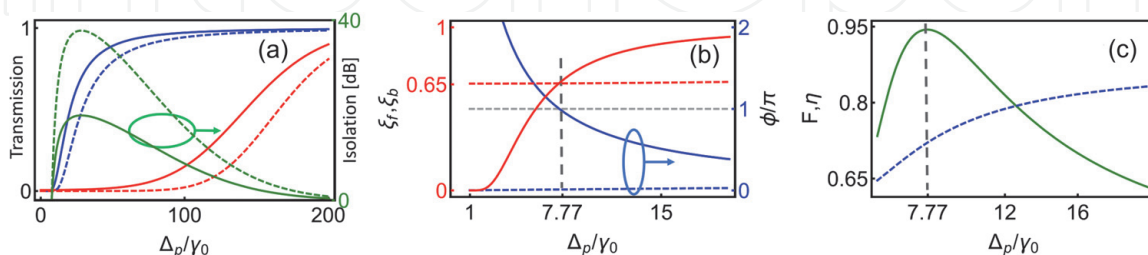


Figure 11.

(a) The transmission of the isolator for forward-moving (blue curves) and backward-moving (red curves) probe fields as a function of the probe detuning Δ_p . Green curves are for the isolations. Solid (dashed) curves are for the length of medium $L = 2(4)$ cm. (b) Amplitude transmissions (red curves) and phase shifts (blue curves) for forward-moving (solid curves) and backward-moving (dashed curves) probe fields as a function of Δ_p . (c) Green curves are for fidelities, and blue dashed curves are for average insertion loss as a function of Δ_p . The vertical black dashed lines in the two figures show the optimal detuning $\Delta_p^{\text{opt}} = 7.77\gamma_0$. The length of medium is 3.33 mm. Other parameters $N_a = 5 \times 10^{12} \text{ cm}^{-3}$, $\Gamma_3 = 0.1\gamma_0$, $\Omega_c = 20\gamma_0$, $\Omega_s = 4\gamma_0$, and $\delta = 0$ are fixed. Reproduced with permission from [20].

the optimal value of π . At the same time, $\xi_f^{\text{opt}} \approx \xi_b^{\text{opt}} \approx 0.66$. As a result, a high-performance circulator can be realized by inserting this nonlinear medium into a MZI composed of unbalanced BSs. In the lower waveguide, a phase shift $\vartheta = 0.01\pi$ is added to compensate the phase shift of the backward-moving photon in the upper one. As shown in **Figure 11c**, when the detuning Δ_p varies from $6\gamma_0$ to $20\gamma_0$, the fidelity \mathcal{F} first rises up rapidly, reaches the maximum 0.944 at $\Delta_p^{\text{opt}} = 7.77\gamma_0$, and then decreases. At the same time, the average photon survival probability η increases from 0.68 to 0.83. Although the photons have a larger probability to survive at a large detuning, the fidelity is low. Thus, there is a trade-off between the fidelity and the survival probability. The circulator operating within the frequency range $6.6\gamma_0 < \Delta_p < 9.7\gamma_0$ can achieve a fidelity larger than 0.9 at the expense of $\eta > 0.69$. The corresponding working window is about $2\pi \times 20$ MHz, and the average insertion loss is about 1.6 dB. At the Δ_p^{opt} , it obtains a fidelity $\mathcal{F} = 0.944$ and a survival probability $\eta = 0.72$, yielding an insertion loss of 1.42 dB. The circulator can also be quantified by the isolations $\{\mathcal{F}_i\} = \{41.7, 13.8, 13.8, 8.2\}$ dB with $i = \{1, 2, 3, 4\}$ (see Eq. (7)), implying nonreciprocal photon circulator along $1 \rightarrow 2 \rightarrow 3 \rightarrow 4 \rightarrow 1$.

The proposal can achieve the nonlinear optical isolation without dynamic reciprocity [36], because the XKerr nonlinearity itself is chiral and the isolation is based on linear equations [20]. According to this proposed method, the device that uses XKerr nonlinearity to achieve cavity-free optical isolator and circulator at ultralow light level has been demonstrated experimentally [21].

5. Conclusions

In this chapter, we introduce the optical chirality of light confined around nanophotonic structures and the chiral optical XKerr nonlinearity induced in atoms. Based on optical chirality, we propose single-photon isolators and circulators with chiral light-emitter interaction. These concepts have been demonstrated experimentally. Then we showed approaches to achieve an optical isolator and a circulator by using the chiral XKerr nonlinearity. All of these approaches can realize chip-comparable optical isolations with low insertion loss and high isolation performance. The methods also work at ultralow light level and even single-photon level. These optical isolators and circulators may pave the way for photon routing and information processing in a nonreciprocal way in integrated optical circuits and quantum networks.

Acknowledgements

K. X. thanks the support of the National Key R&D Program of China (Grant No. 2017YFA0303703) and the National Natural Science Foundation of China (Grants Nos. 11874212 and 61435007). He also thanks his co-workers, in particular, Prof. Jason Twamley, Prof. Yong Zhang, Prof. Min Xiao, and Prof. Franco Nori for their essential contribution to the original works.

Abbreviations

OC	optical chirality
WGM	whispering-gallery mode

QD	quantum dot
OSE	optical Stark effect
CCW	counterclockwise
CW	clockwise
FDTD	finite-difference time-domain
XKerr	cross-Kerr
MZI	Mach-Zehnder interferometer
BS	beam splitter

IntechOpen

Author details

Lei Tang^{1,2,3*†} and Keyu Xia^{1,2,3†}

1 College of Engineering and Applied Sciences, Nanjing University, Nanjing, China

2 National Laboratory of Solid State Microstructures, Collaborative Innovation Center of Advanced Microstructures, Nanjing University, Nanjing, China

3 Jiangsu Key Laboratory of Artificial Functional Materials, and Key Laboratory of Intelligent Optical Sensing and Manipulation, Ministry of Education, Nanjing University, Nanjing, China

*Address all correspondence to: tanglei@smail.nju.edu.cn

† These authors contributed equally.

IntechOpen

© 2019 The Author(s). Licensee IntechOpen. This chapter is distributed under the terms of the Creative Commons Attribution License (<http://creativecommons.org/licenses/by/3.0>), which permits unrestricted use, distribution, and reproduction in any medium, provided the original work is properly cited. 

References

- [1] Cirac JI, Zoller P, Kimble HJ, Mabuchi H. Quantum state transfer and entanglement distribution among distant nodes in a quantum network. *Physical Review Letters*. 1997;**78**(16):3221-3224. DOI: 10.1103/PhysRevLett.78.3221
- [2] Kimble HJ. The quantum internet. *Nature*. 2008;**453**(7198):1023-1030. DOI: 10.1038/nature07127
- [3] Hacker B, Welte S, Remppe G, Ritter S. A photon-photon quantum gate based on a single atom in an optical resonator. *Nature*. 2016;**536**(7615):193-196. DOI: 10.1038/nature18592
- [4] Riedinger R, Hong S, Norte RA, Slater JA, Shang J, Krause AG, et al. Non-classical correlations between single photons and phonons from a mechanical oscillator. *Nature*. 2016;**530**(7590):313-316. DOI: 10.1038/nature16536
- [5] Sathyamoorthy SR, Tornberg L, Kockum AF, Baragiola BQ, Combes J, Wilson CM, et al. Quantum nondemolition detection of a propagating microwave photon. *Physical Review Letters*. 2014;**112**(9):093601. DOI: 10.1103/PhysRevLett.112.093601
- [6] Bi L, Hu J, Jiang P, Kim DH, Dionne GF, Kimerling LC, et al. On-chip optical isolation in monolithically integrated non-reciprocal optical resonators. *Nature Photonics*. 2011;**5**(12):758-762. DOI: 10.1038/NPHOTON.2011.270
- [7] Tien MC, Mizumoto T, Pintus P, Kromer H, Bowers JE. Silicon ring isolators with bonded nonreciprocal magneto-optic garnets. *Optics Express*. 2011;**19**(12):11740-11745. DOI: 10.1364/OE.19.011740
- [8] Fan L, Wang J, Varghese LT, Shen H, Niu B, Xuan Y, et al. An all-silicon passive optical diode. *Science*. 2012;**335**(6067):447-450. DOI: 10.1126/science.1214383
- [9] Peng B, Özdemir Ş K, Lei F, Monifi F, Gianfreda M, Long GL, et al. Parity-time-symmetric whispering-gallery microcavities. *Nature Physics*. 2014;**10**(5):394-398. DOI: 10.1038/NPHYS2927
- [10] Chang L, Jiang X, Hua S, Yang C, Wen J, Jiang L, et al. Parity-time symmetry and variable optical isolation in active-passive-coupled microresonators. *Nature Photonics*. 2014;**8**(7):524-529. DOI: 10.1038/NPHOTON.2014.133
- [11] Ruesink F, Miri MA, Alu A, Verhagen E. Nonreciprocity and magnetic-free isolation based on optomechanical interactions. *Nature Communications*. 2016;**7**:13662. DOI: 10.1038/ncomms13662
- [12] Shen Z, Zhang YL, Chen Y, Zou CL, Xiao YF, Zou XB, et al. Experimental realization of optomechanically induced non-reciprocity. *Nature Photonics*. 2016;**10**(10):657-661. DOI: 10.1038/NPHOTON.2016.161
- [13] Fang K, Luo J, Metelmann A, Matheny MH, Marquardt F, Clerk AA, et al. Generalized non-reciprocity in an optomechanical circuit via synthetic magnetism and reservoir engineering. *Nature Physics*. 2017;**13**(5):465-471. DOI: 10.1038/NPHYS4009
- [14] Dong MX, Yu YC, Ye YH, Zhang WH, Li EZ, Zeng L, et al. Experimental realization of quantum non-reciprocity based on cold atomic ensembles. arXiv:1908.09242v1. 2019. <https://arxiv.org/abs/1908.09242v1>
- [15] Lodahl P, Mahmoodian S, Stobbe S, Rauschenbeutel A, Schneeweiss P, Volz J, et al. Chiral quantum optics. *Nature*. 2017;**541**(7638):473-480. DOI: 10.1038/nature21037

- [16] Xia K, Lu G, Lin G, Cheng Y, Niu Y, Gong S, et al. Reversible nonmagnetic single-photon isolation using unbalanced quantum coupling. *Physical Review A*. 2014;**90**(4):043802. DOI: 10.1103/PhysRevA.90.043802
- [17] Tang L, Tang J, Zhang W, Lu G, Zhang H, Zhang Y, et al. On-chip chiral single-photon interface: Isolation and unidirectional emission. *Physical Review A*. 2019;**99**(4):043833. DOI: 10.1103/PhysRevA.99.043833
- [18] Sayrin C, Junge C, Mitsch R, Albrecht B, O'Shea D, Schneeweiss P, et al. Nanophotonic optical isolator controlled by the internal state of cold atoms. *Physical Review X*. 2015;**5**(4):041036. DOI: 10.1103/PhysRevX.5.041036
- [19] Scheucher M, Hilico A, Will E, Volz J, Rauschenbeutel A. Quantum optical circulator controlled by a single chirally coupled atom. *Science*. 2016;**354**(6319):1577-1580. DOI: 10.1126/science.aaj2118
- [20] Xia K, Nori F, Xiao M. Cavity-free optical isolators and circulators using a chiral cross-Kerr nonlinearity. *Physical Review Letters*. 2018;**121**(20):203602. DOI: 10.1103/PhysRevLett.121.203602
- [21] Li EZ, Ding DS, Yu YC, Dong MX, Zeng L, Zhang WH, et al. Experimental demonstration of cavity-free optical isolators and optical circulators. *arXiv:1908.07210v1*. 2019. <https://arxiv.org/abs/1908.07210v1>
- [22] Mahmoodian S, Prindal-Nielsen K, Sölner I, Stobbe S, Lodahl P. Engineering chiral light-matter interaction in photonic crystal waveguides with slow light. *Optical Materials Express*. 2017;**7**(1):43-51. DOI: 10.1364/OME.7.000043
- [23] Shen Y, Bradford M, Shen JT. Single-photon diode by exploiting the photon polarization in a waveguide. *Physical Review Letters*. 2011;**107**(17):173902. DOI: 10.1103/PhysRevLett.107.173902
- [24] Shen JT, Fan S. Coherent photon transport from spontaneous emission in one-dimensional waveguides. *Optics Letters*. 2005;**30**(15):2001-2003. DOI: 10.1364/OL.30.002001
- [25] Turchette QA, Hood CJ, Lange W, Mabuchi H, Kimble HJ. Measurement of conditional phase shifts for quantum logic. *Physical Review Letters*. 1995;**75**(25):4710. DOI: 10.1103/PhysRevLett.75.4710
- [26] Junge C, O'shea D, Volz J, Rauschenbeutel A. Strong coupling between single atoms and nontransversal photons. *Physical Review Letters*. 2013;**110**(21):213604. DOI: 10.1103/PhysRevLett.110.213604
- [27] Xu X, Sun B, Berman PR, Steel DG, Bracker AS, Gammon D, et al. Coherent population trapping of an electron spin in a single negatively charged quantum dot. *Nature Physics*. 2008;**4**(9):692-695. DOI: 10.1038/nphys1054
- [28] Vetsch E, Reitz D, Sagué G, Schmidt R, Dawkins ST, Rauschenbeutel A. Optical interface created by laser-cooled atoms trapped in the evanescent field surrounding an optical nanofiber. *Physical Review Letters*. 2010;**104**(20):203603. DOI: 10.1103/PhysRevLett.104.203603
- [29] Choi BH, Park CM, Song SH, Son MH, Hwang SW, Ahn D, et al. Selective growth of InAs self-assembled quantum dots on nanopatterned SiO₂/Si substrate. *Applied Physics Letters*. 2001;**78**(10):1403-1405. DOI: 10.1063/1.1352049
- [30] Atatüre M, Dreiser J, Badolato A, Högele A, Karrai K, Imamoglu A. Quantum-dot spin-state preparation with near-unity fidelity. *Science*. 2006;**312**(5773):551-553. DOI: 10.1126/science.1126074

[31] Vora PM, Bracker AS, Carter SG, Sweeney TM, Kim M, Kim CS, et al. Spin–cavity interactions between a quantum dot molecule and a photonic crystal cavity. *Nature Communications*. 2015;**6**:7665. DOI: 10.1038/ncomms8665

[32] Yong CK, Horng J, Shen Y, Cai H, Wang A, Yang CS, et al. Biexcitonic optical stark effects in monolayer molybdenum diselenide. *Nature Physics*. 2018;**14**(11):1092-1096. DOI: 10.1038/s41567-018-0216-7

[33] Htoon H, Takagahara T, Kulik D, Baklenov O, Holmes AL Jr, Shih CK. Interplay of Rabi oscillations and quantum interference in semiconductor quantum dots. *Physical Review Letters*. 2002;**88**(8):087401. DOI: 10.1103/PhysRevLett.88.087401

[34] Shen JT, Fan S. Theory of single-photon transport in a single-mode waveguide. II. Coupling to a whispering-gallery resonator containing a two-level atom. *Physical Review A*. 2009;**79**(2):023838. DOI: 10.1103/PhysRevA.79.023838

[35] Söllner I, Mahmoodian S, Hansen SL, Midolo L, Javadi A, Kiršanskė G, et al. Deterministic photon–emitter coupling in chiral photonic circuits. *Nature Nanotechnology*. 2015;**10**(9):775-778. DOI: 10.1038/NNANO.2015.159

[36] Shi Y, Yu Z, Fan S. Limitations of nonlinear optical isolators due to dynamic reciprocity. *Nature Photonics*. 2015;**9**(6):388-392. DOI: 10.1038/NPHOTON.2015.79